IAC–20–C2.9

CubeSat Magnetic Atlas and in-Orbit Compensation of Residual Magnetic Dipole

Anastasiia Annenkova
Skolkovo Institute of Science and Technology, Russian Federation, Anastasiia.Annenkova@skoltech.ru

Nourhan Abdelrahman
Skolkovo Institute of Science and Technology, Russian Federation, Nourhan.Abdelrahman@skoltech.ru

Danil Ivanov
Keldysh Institute of Applied Mathematics, RAS, Russian Federation, danilivanovs@gmail.com

Dmitry Roldugin
Keldysh Institute of Applied Mathematics, RAS, Russian Federation, rolduginds@gmail.com

Dmitry Pritykin
Skolkovo Institute of Science and Technology, Russian Federation, d.pritykin@skoltech.ru

Abstract

Magnetic cleanliness and in-flight identification and rejection of residual magnetization effects for a magnetically controlled 3U CubeSat are considered. The routine we propose starts from accurate acquisition of all the components' magnetic fields at the stage when the engineering model of the spacecraft is ready. This allows making a map of the assembled CubeSat's internal magnetic fields using electromagnetic simulation and analysis software. Such maps can be produced for each operational regime of the spacecraft and compose a magnetic atlas in accordance with the concept of operations. By feeding the maps to the extended Kalman filter, which processes the magnetometer data and estimates the residual magnetic dipole and the magnetometer bias along with the state variables, we ensure a better initial guess for the disturbances, which is crucial for the filter's convergence. It is shown to be of importance, whenever the level of magnetic disturbances abruptly changes as the spacecraft switches between the regimes.
keywords: CubeSat, magnetic control, residual magnetization, disturbance identification

1. Introduction

This study has been conducted as a part of the Skoltech University project to deploy a swarm of four 3U CubeSats in LEO. The principal objective of the mission is collective gamma-ray bursts detection, which assumes coordinated attitude determination and control of the spacecraft in the swarm [10]. Magnetic control is a frequent choice for CubeSat missions when pointing requirements – and such is the case for the mission we consider – are not very demanding. Magnetic actuators are admittedly low cost, relatively simple to manufacture, and the research on their use in the attitude control loop is abundant. It has been shown, however, that for spacecraft with small moments of inertia a major disturbance that significantly degrades attitude control accuracy is due to residual magnetization [7]. Furthermore, prior research [2] indicates that even perfect identification of the residual magnetic dipole does not allow its full compensation for larger values of the magnetic dipoles in CubeSats that are reported in the literature [15].

Magnetic disturbances have concerned many satellite missions over the lifetime of space industry, whether for purposes of surrounding field data studies as in CASSINI[3] and THEMIS[9] or for purposes of attitude control [5]. Electromagnetic compatibility tests and magnetic cleanliness techniques were developed to face this issue [13] and implemented by space agencies. These techniques appear to be sufficient for most of the large missions. It has been shown, however, that the level of residual magnetization can change during the spacecraft's lifetime, and can significantly affect the rotational dynamics of the observed defunct satellites in LEO [12]. This implies that even for large spacecraft the residual magnetization can become one of the governing factors in rota-

tional dynamics that must not be overlooked. More so, for a LEO CubeSat that plans to use magnetic control, the disturbances due to residual magnetization become critical and require utmost attention during design, assembly and operation phases.

There are two factors to consider in magnetic attitude determination and control: Earth's magnetic field measurement through magnetometer and control through magnetorquers. Disturbances affect both sides as residual magnetic field of the satellite is measured in the first step and torque due to residual magnetization distorts the control action in the second step.

Through this work, a complement procedure to electromagnetic cleanliness routines [13] is proposed in which residual magnetization effects are assessed, mitigated and mapped in various stages of the CubeSat lifecycle. An under development CubeSat design is used to build a software model that would calculate the magnetic field and torque parameters due to printed circuit boards (PCB) and solar panel (these are selected to exemplify the procedure). The software model is to be verified using hardware measurements until its accuracy is ensured. The field values from the model are then imported to a simulation of the control algorithm implementing extended Kalman filter to check the spacecraft controllability and consequent need to further mitigate the disturbance.

The paper has the following structure. Section 2 describes the general electromagnetic cleanliness routines, briefly overviews the physics of residual magnetization and defines the model we employ to capture its effects. The Section ends with the results obtained for the existing design of PCBs and solar panels. Section 3 introduces the model of the spacecraft rotational dynamics and the adopted onboard algorithm to identify and reject the magnetic disturbances. The same algorithm is used while still on the ground to construct the maps for principal operational regimes of the spacecraft, by estimating magnetometer bias and torque due to residual magnetization. Section **??** presents the simulation results and shows how the usage of the atlas enhances attitude determination and control routines. Finally, the Conclusion offers a discussion of the obtained results and delineates future work.

2. Residual Magnetization

2.1 *Electromagnetic cleanness*

Stable magnetic control requires accurate measurements and precise extended Kalman filter state estimates. For a CubeSat with a preliminary design, sources of magnetization are neither known nor limited which leads to their interference the control loop and causes the controller to diverge. According to ECSS standards [13], the study of a spacecraft's level of magnetization is called 'Electromagnetic compatibility program'. The purpose of the program is to ensure that the magnetic field at sensitive points (i.e magnetometer or sensitive payloads) is limited and modelled so its effect is known and can be removed. Many satellites such as SELENE[11], THEMIS[9], CASSINI[3], etc.. have been reported to follow such programs. The steps of the program can be summarized into a few points:

1. definition of a tolerance range for magnetic field at certain vulnerable points along with the corresponding admissible level of residual magnetization;
2. identification of main sources that produce magnetic field;
3. establishment of a general plan in all subsystems to minimize the sources and their effect;
4. measurements of subsystems magnetic field along with the overall satellite magnetic field at the sensitive points to monitor the change due to the program and confirm that it is within the established limits;
5. repetition of the above procedure in a loop until the required levels of magnetic field and residual magnetization are obtained.

The categorization of the magnetic disturbances' sources can be represented as [8]:

1. frequency operating components especially high frequency ones which in terms of values are higher than 10 Hz (i.e converters, power electronics components (switches, transistors, capacitors), motors, antennas and modems);
2. current flow through the components and wires;
3. static charge accumulated in satellite parts especially strongly magnetizable materials (soft magnetic materials);
4. AC/DC sources.

After the identification of the sources, minimization methods range between shielding parts, replacing soft magnetic material with hard magnetic materials (harder to get magnetized), applying symmetry

plans in subsystem placement and in wiring to have cancellation effects (i.e double wiring some of the high current carrying wires) and addition of magnetic elements to cancel the effect of other sources.

This procedure, when fully implemented, is known to produce an acceptable accuracy for large satellites [3, 9, 11]. Small CubeSats however – for various reasons – are not always taken through a thorough magnetic cleanliness procedure, which circumstance may and often does result in poor controllability. Thus, a model of detailed distribution of magnetic field is required. In the following sections, field due to specific components of the satellite is to be calculated. We focus on the electric power subsystem (EPS) components as they tend to have one of the most significant effects. Additionally, seeing how current paths could be the hardest to model and yet the most abundant in terms of parasitic magnetic field, they were the ones to be handled. Other sources such as soft magnetic materials have a different process of elimination that could only be done through measurements. The rest of the sources and the model of the full satellite are intentionally left beyond the scope of this paper as our goal here is only to outline the pipeline of our tentative CubeSat magnetic cleanliness program.

2.2 *Physics*

As speculated earlier, the atlas build requires obtaining two quantities: the magnetic field and the torque due to residual magnetization.

Biot-Savart law calculates the magnetic field produced by a current-carrying wire as follows:

$$\mathbf{b} = \frac{\mu_0}{4\pi} I \int d\mathbf{L} \times \frac{\mathbf{r}}{r^3} \tag{1}$$

with $\mathbf{b}$ as the magnetic field, μ_0 the magnetic permeability of space, I is the current going through the wire, $d\mathbf{L}$ is a vector segment of the wire and $\mathbf{r}$ is the vector from the point of field calculation to the middle point of the wire segment. This covers the first input parameter needed.

The torque due to residual magnetization is often described using another quantity – residual magnetic moment, which is expressive of the magnetization strength of a magnetic producing part. Unlike magnetic field, residual magnetic moment does no depend on the observation point. The following equation calculates the torque $\mathbf{T}$ acting upon a satellite having a residual magnetic moment vector $\mathbf{m}$ and immersed into an external magnetic field $\mathbf{b}_{ext}$:

$$\mathbf{T} = \mathbf{m} \times \mathbf{b}_{ext}. \tag{2}$$

For a single planar closed loop of wire, RMM can be calculated as

$$m = I \cdot A \tag{3}$$

where I is the current going through the loop and A is the area of the loop.For a planar loop, $\mathbf{m}$ is perpendicular to the plane of the loop. Alternately, if the current is still confined to a closed circuit:

$$\mathbf{m} = \frac{1}{2} \int \mathbf{r} \times d\mathbf{I} \tag{4}$$

This definition cannot be applied to the case under study because of the closed-circuit assumption. The assumption removes the effect of forces in the torque calculation as for closed loops the total magnetic force is zero. That, however, is not the case for a PCB of solar panels, where forces do not cancel each other out and thus should be taken into account.

Thus, another representation of torque and RMM is adopted. Elementary force $d\mathbf{F}$ and torque $d\mathbf{T}$ acting upon a current-carrying wire due to a surrounding magnetic field are given by:

$$d\mathbf{F} = I(d\mathbf{L} \times \mathbf{b}_{ext}) \tag{5}$$

$$d\mathbf{T} = \mathbf{r} \times (Id\mathbf{L} \times \mathbf{b}_{ext}) \tag{6}$$

Let us introduce for any vector $\mathbf{a} = (a_x, a_y, a_z)^T$ a skew-symmetric matrix as:

$$\mathbb{W}_{\mathbf{a}} = \begin{bmatrix} 0 & -a_z & a_y \\ a_z & 0 & -a_x \\ -a_y & a_x & 0 \end{bmatrix} \tag{7}$$

Expressing vectors $\mathbf{r}$ and $\mathbf{IL}$ as skew matrices changes the equation 6 to:

$$\mathbf{T}_{total} = \mathbb{M} \cdot \mathbf{b}_{ext}, \tag{8}$$

where

$$\mathbb{M} = \sum \mathbb{W}(\mathbf{r})\mathbb{W}(Id\mathbf{L}). \tag{9}$$

$\mathbb{M}$ will be further referred to as torque matrix because it can be used to calculate the torque acting on the satellite due to external magnetic field as in equation (8). This matrix is reference-point dependant and unless specified otherwise it will be calculated for the spacecraft's center of mass. This matrix is descriptive of residual magnetization of any component within the spacecraft in terms of torque it produces and thus covers the second quantity required for the model.

The work was done on an under development 3U CubeSat with known positions and designs for the

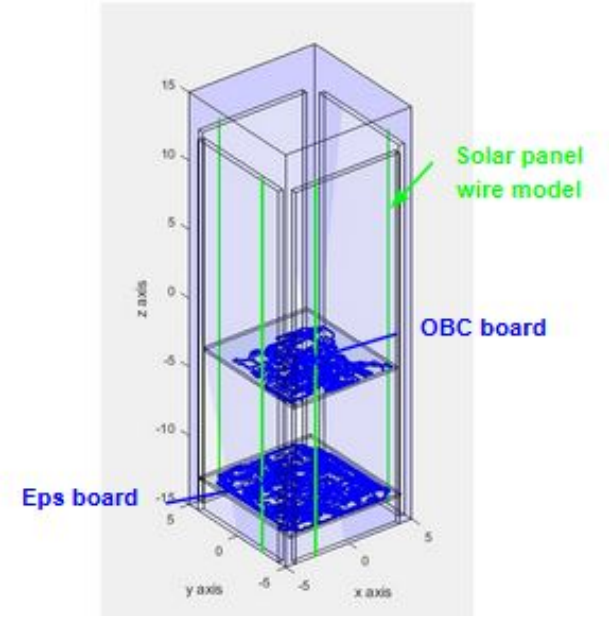

Fig. 1: Cubesat with positioned components

components to be analysed as in Fig. 1. The studied components belong mainly to EPS as it is usually the one carrying the most significant currents. The placed components are its PCB, solar panels and onboard computer PCB. Their full size placements could be seen as the transparent boxes inside the satellite. Their representative wires are marked in blue for the PCBs and in green for the solar panels.

The analysis and assumption for PCBs and solar panels were carried out separately and are presented in the following paragraphs.

PCBs were imported from Altium software (see Fig. 2). As much as it is helpful in design, it is not specialized in field and torque design so another software was needed for the task. MATLAB was a good choice and it was possible to use through the import of Gerber files from Altium with the aid of a preexisting library [4]. Nonetheless, the import had only the tracks of the PCB but not the components, currents' values or directions. The read files were plotted in MATLAB to result in what is seen in Fig. 3.

Because some of the information was missing in the imported Gerber files, assumptions were made to facilitate the calculations. The assumptions are:

1. Current flows from on side of the PCB to the other side in all tracks. This first side is defined to be the one where the power source is placed and the second side is the opposing one.

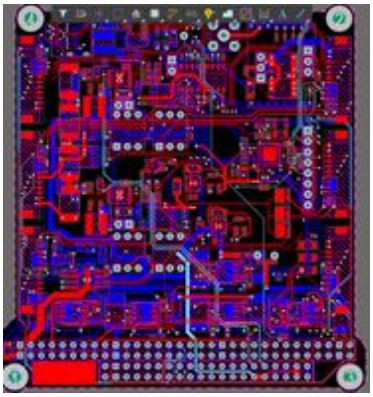

Fig. 2: Altium PCB design

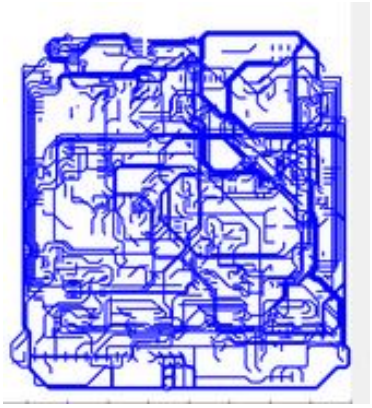

Fig. 3: MATLAB PCB tracks plot

Fig. 4: PCB detected tracks

2. Given the main current input to the whole PCB and the thickness of all tracks, an assumption was made that the maximum current would pass through the thickest track. The current passing through the rest of the tracks would be a ration

in their thickness calculated from maximum current input and maximum track width.

3. Each track follows a one direction and contains no branching within.

Using these assumptions, several tracks were detected but others were not. In Fig. 4, the red tracks are the detected ones from the overall PCB tracks shown in blue.

Now that all inputs for PCB definition are defined, it is possible to proceed to field an torque calculations.

Solar Panels contribute with a considerable amount in CubeSat's magnetic field. That is because it is the main source of power during the Sun exposure. Due to this the effect of the panels is calculated. On the other hand, batteries, being a power source during eclipse, were not considered as their magnetic field contribution occurs only through the connection wires which are left for a later study.

To model the solar panels we adopted the approach described in [14], where wires representation was considered and each solar cell in the panel was replaced with a single wire connected from both sides to the wires of other cells. The resulting model is shown in Fig. 1 as the green wires.

Magnetic Field Distribution was calculated for all points within the CubeSat to reach a conclusion about the least affected positions of the satellite with the currently analysed components.

The results are divided into two modes: Constant valued PCBs in Fig. 5 and varying solar panels due to the change of the sunlight incidence angle seen in Fig. 6, 7.

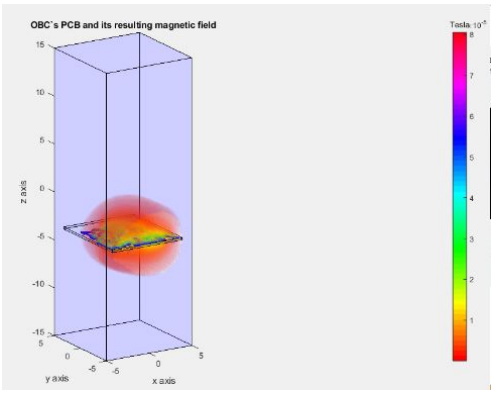

Fig. 5: Magnetic field distribution due to OBC PCB

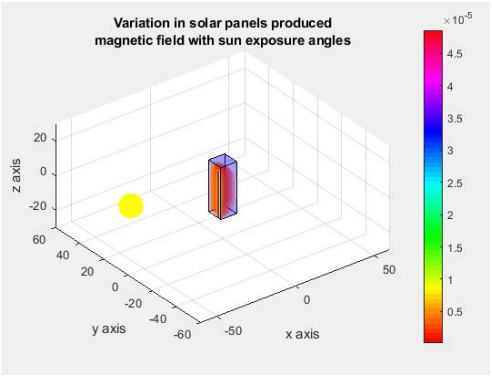

Fig. 6: Varying magnetic field due to sun incidence angle on solar panels

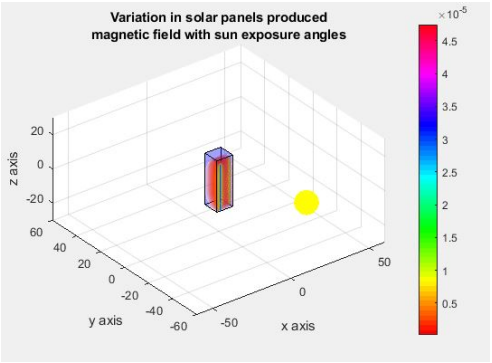

Fig. 7: Varying magnetic field due to sun incidence angle on solar panels

The values were only recorded at the points that were chosen to have the magnetometer at and imported to extended Kalman filter model.

3. Attitude control

3.1 *Reference frames*

The following reference frames will be used:

1. The Earth-Centered Inertial reference frame (ECI) $\mathcal{F}^I$, whose origin is at the Earth's center and axes coincide with those of the J2000 frame.

2. The Orbital reference frame $\mathcal{F}^O$, whose origin is at the center of mass of the satellite, z-axis pointing away from the center of the Earth, y-axis along the cross product of the satellite's center of mass position and velocity vectors, and x-axis completing the frame according to the right hand rule.

3. The Body-fixed reference frame $\mathcal{F}^B$ with the origin at the satellite's center of mass. Its three axes

are assumed to coincide with the three principal axes of inertia of the satellite.

All vector transformations are given in the quaternion notation. A quaternion q^{YX} is said to relate two reference frames $\mathcal{F}^X$ and $\mathcal{F}^Y$ if representations of any given vector r in these frames are related by:

$$\mathbf{r}^Y = q^{YX} \circ \mathbf{r}^X \circ \tilde{q}^{YX} \tag{10}$$

3.2 *Equations of Motion*

According to the results of the preliminary design [1] the CubeSats in consideration will have no deployables. Thus, the modelled satellite is further assumed to be rigid body with a constant inertia tensor. Under this assumption, the rotational motion can be described by the Poisson's and Euler's equations:

$$\dot{q}^{OB} = \frac{1}{2} q^{OB} \circ \boldsymbol{\Omega}^B, \tag{11}$$

$$\mathbb{J}^B \dot{\boldsymbol{\omega}}^B + \boldsymbol{\omega}^B \times \mathbb{J}^B \boldsymbol{\omega}^B = \boldsymbol{T}^B_{ext}, \tag{12}$$

where q^{OB} is the unit quaternion that transforms any vector from the $\mathcal{F}^B$ frame to the $\mathcal{F}^O$ frame, $\boldsymbol{\omega}$ is the absolute angular velocity of the satellite (projected onto the body-frame), $\mathbb{J}$ is the tensor of inertia of the satellite, $\mathbb{J}^B = \mathrm{diag}\,(A,\ B,\ C)$, $\boldsymbol{T}_{ext}$ is the external torque acting on the satellite, $\boldsymbol{\Omega}^B$ is the satellite's angular velocity with respect to the $\mathcal{F}^O$ frame:

$$\boldsymbol{\Omega}^B = q^{BO} \circ \begin{bmatrix} 0 & \omega_0 & 0 \end{bmatrix}^\top \circ \tilde{q}^{BO} - \boldsymbol{\omega}^B, \tag{13}$$

where ω_0 is the mean motion of the satellite in orbit. All vectors in Eq. (13) are written in the $\mathcal{F}^B$ frame.

In all subsequent simulation we start from random initial conditions. The initial state quaternion q^{OB}_{in} is generated as a random four-dimensional vector (and then normalized), the initial angular velocity ω_{in} is also a randomly generated vector, whose absolute value does not exceed 5 deg/s.

3.3 *Environment*

In the course of preliminary studies [1, 10] estimates have been carried out to determine the order of magnitude of the environmental torques that may act on a 3U CubeSat. Four sources of environmental torques have been estimated: gravity-gradient torque, aerodynamic drag torque, solar radiation pressure torque, and the torque due to residual magnetization. Taking into account available data on 3U CubeSat residual magnetic dipole [15], which can be as large as $\mathbf{m}_{res} = 0.01$ A·m^2, we conclude that magnetic disturbance may indeed become the dominant source of attitude determination and control errors.

Based on the estimates it is decided to include into the right-hand side of the Equations (12) as constituents of $\boldsymbol{T}^B_{ext}$ torques due to gravity and residual magnetization, whereas all other environmental torques will be modeled as normally distributed random variable $\boldsymbol{T}^B_{dist}$. The models for the former torques as well as the parameters for the normal distribution for the latter torques are specified below.

Gravity-gradient torque The gravity-gradient torque is given by the formula:

$$\boldsymbol{T}_{grav} = 3\omega_0^2 \left(\mathbf{e}_o^B \times \mathbb{J}\mathbf{e}_o^B\right), \tag{14}$$

where $\mathbf{e}_o^B$ is the unit vector from the center of the gravity field to the body's center of mass.

Residual magnetization From the calculations made in the Section 2.2, we are getting constant matrices of CubeSat's residual magnetization from PCBs, such as EPS ans OBC: $\mathbb{M}_{EPS}$, $\mathbb{M}_{OBC}$ and $\mathbf{M}_{sun}$. It must be noted, that the latter matrix is computed for the maximum possible current in the solar panel and thus when used in the magnetization model it should be rescaled as the current in the ith solar panel is proportional to the $\cos\alpha_i$, where α_i is the incident angle of sunlight (see Fig. 8).

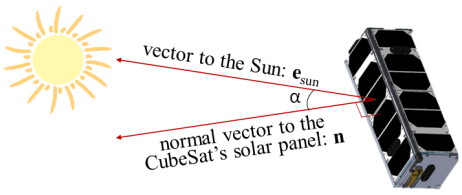

Fig. 8: Varying residual magnetization of solar panels due to sun incidence angle on solar panels

Thus the total torque matrix $\mathbb{M}_{res}$ is modeled as:

$$\mathbb{M}_{res} = \mathbb{M}_{EPS} + \mathbb{M}_{OBC} + \\ + \psi \cdot \sum_{i=1}^{4} \max\left(0, \cos\alpha_i\right) \cdot \mathbb{M}_{sun}, \tag{15}$$

where the factor $\max\left(0, \cos\alpha_i\right)$ is used to indicate that only those panel have current running through them that are lit by the Sun, $\psi \in \{0, 1\}$ is the Earth's shadow indicator function.

Magnetic torque The torque acting upon a body, whose magnetization consists of control moment $\mathbf{m}_{ctrl}$ and residual magnetization from components $\mathbb{M}_{res}$ in the Earth's magnetic field $\mathbf{b}$ is

$$\mathbf{T}_m = \mathbf{m}^B_{ctrl} \times \mathbf{b}^B + \mathbb{M}_{res} \cdot \mathbf{b}^B, \tag{16}$$

where $\mathbf{b}^B$ is the local geomagnetic field vector represented in the $\mathcal{F}^B$ frame.

Geomagnetic field representations Three different representations of the geomagnetic field are used in the subsequent simulations:

- **the on-board model** $\mathbf{b}_{model}$, which is generating the magnetic field representation within the attitude determination loop of the ADCS using direct dipole model as follows [6]:

$$\mathbf{b}^O_{model} = \frac{\mu_0 \mu_E}{4\pi R_o^3} \begin{bmatrix} \cos u \sin i \\ \cos i \\ -2 \sin u \sin i \end{bmatrix} \tag{17}$$

  where $\mu_0 \approx 1.257 \cdot 10^{-6}$ N $\cdot$ A^{-2} is the magnetic permeability of free space, $\mu_{\mathrm{E}} \approx 7.94 \cdot 10^{22}$ A$\cdot$m^2 is the magnetic dipole moment of the Earth, R_o is the orbit radius, i is the inclination of the orbit, and u is the argument of latitude.

- **the actual magnetic field** of the Earth $\mathbf{b}_{env}$ as the satellite's environment is modeled to differ from the one computed by the on-board model by a normally distributed random vector:

$$\begin{aligned} \mathbf{b}^O_{env} &= \mathbf{b}^O_{model} + \mathbf{r}_{env}, \\ \mathbf{r}_{env} &\sim \mathcal{N}_3 \left(\boldsymbol{\mu}_{env}, \boldsymbol{\Sigma}_{env} \right) \end{aligned} \tag{18}$$

  where the parameters of the random vector $\mathbf{r}_{env}$ are set to $\boldsymbol{\mu}_{env} = 10^{-8} \cdot \begin{bmatrix} 1 & 1 & 1 \end{bmatrix}^\top$ T and $\boldsymbol{\Sigma}_{env} = \left(2 \cdot 10^{-8}\right)^2 \cdot \mathbb{I}_{3\times 3}$.

- the magnetic field $\mathbf{b}_{sens}$ as measured by the satellite's **on-board sensors**:

$$\begin{aligned} \mathbf{b}^B_{sens} &= \mathbf{b}^B_{env} + \mathbf{r}_{sens}, \\ \mathbf{r}_{sens} &\sim \mathcal{N}_3 \left(\boldsymbol{\mu}_{sens}, \boldsymbol{\Sigma}_{sens} \right) \end{aligned} \tag{19}$$

  where variance of the random vector $\mathbf{r}_{sens}$ is set to $\boldsymbol{\Sigma}_{sens} = \left(2 \cdot 10^{-7}\right)^2 \cdot \mathbb{I}_{3\times 3}$, whereas μ_{sens} should take into account the influence of the satellites' residual magnetization in accordance with the model for the parasitic magnetic field $\mathbf{b}_res$ induced at the location of the magnetometer as given in Section 2.2.

3.4 *Control Algorithm*

The Lyapunov-based control algorithm [6] is considered to align the $\mathcal{F}^B$ frame with the $\mathcal{F}^O$ frame as a mission requirement. The control magnetic moment to be generated by the actuators is computed in the beginning of each control loop as

$$\mathbf{m}^B_{ctrl\_PD} = -k_\omega \mathbf{b}^B_{est} \times \boldsymbol{\Omega}^B - k_q \mathbf{b}^B_{est} \times \mathbf{S} \tag{20}$$

where $\mathbf{b}^B_{est}$ is the processed measurements of the magnetic field $\mathbf{b}^B_{sens}$, $\boldsymbol{\Omega}^B$ is the relative angular velocity of the spacecraft, k_ω and k_q are controller gains, $\mathbf{S}$ is the attitude error between the reference and actual attitudes given by

$$\mathbf{S} = 4 q_0^{OB} \mathbf{q}^{OB} \tag{21}$$

where q_0^{BO} and $\mathbf{q}^{BO}$ are the scalar and vector parts of the unit quaternion q^{BO}.

The disturbance rejection algorithm implies that the estimate of torque due to residual magnetization is obtained and translated into the actuation available from the magnetorquers. Thus, we reject the magnetic disturbance by generating additional magnetic moment:

$$\mathbf{m}^B_{ctrl} = \mathbf{m}^B_{ctrl\_PD} - \mathbf{m}^B_{res}. \tag{22}$$

The algorithm to obtain the estimate of $\mathbf{m}^B_{res}$ is described in Section 3.5.

Each control loop consists of two parts - actuation and measurements, the duration of each part is t_{ctrl} and t_{sens}. During the actuation phase the magnetorquers are generating a constant magnetic moment calculated before the actuation according to Equation (22). After the actuation is over the measurements part starts, during which the magnetorquers are switched off and at the end of this period the sensors data are read and processed.

3.5 *Extended Kalman Filter*

Let us now introduce the extended Kalman filter to estimates the conventional state vector (comprising the attitude quaternion q^{OB} and the angular velocity vector $\boldsymbol{\omega}$) along with residual magnetization effects. The latter include the residual magnetic moment $\mathbf{m}^B_{res}$ (which must be generated by the magnetorquers to cancel out the torque due to residual magnetization) and the magnetometer bias $\mathbf{b}^B_{res}$ due to residual magnetization.

EKF is a recursive estimator with the state evolution and observation models represented by nonlinear equations,

$$\dot{\mathbf{x}}(t) = \mathbf{f}(\mathbf{x}(t)) + \mathbf{w}(t) \tag{23}$$

$$\mathbf{z} = \mathbf{h}(\mathbf{x}(t)) + \mathbf{v}(t) \tag{24}$$

Equations (23) and (24) represent the state evolution and observation models respectively, where $\mathbf{x}(t)$ is the state vector at time t and $\mathbf{z}$ is the measurement vector at the time instant k. $\mathbf{w}(t)$ and $\mathbf{v}(t)$ are the process and observation noises which are assumed to be Gaussian noises with zero means and have $\mathbb{Q}(t)$ and $\mathbb{R}_k$ respectively as covariance matrices.

As specified earlier the state vector the EKF estimates is:

$$\mathbf{x} = \begin{bmatrix} \mathbf{q}^{OB} \\ \boldsymbol{\omega}^{B} \\ \mathbf{m}^{B}_{res} \\ \mathbf{b}^{B}_{res} \end{bmatrix} \tag{25}$$

The evolution model is thus represented by the Equations (11) and (12).

The EKF algorithm is divided into two successive phases, Prediction and Update. In the following equations, the superscript '-' and '+' represents that the value is from Prediction phase or from Update correspondingly: $\hat{\mathbf{x}}_k^-$ - Prediction phase, $\hat{\mathbf{x}}_k^+$ - Update phase. The subscript k and k-1 represents current and previous steps, respectively.

Prediction

$$\hat{\mathbf{x}}_k^- = \int_{t_{k-1}}^{t_k} \mathbf{f}\left(\hat{\mathbf{x}}_{k-1}^+, t\right) dt \tag{26}$$

$$\mathbb{P}_k^- = \boldsymbol{\Phi}_k \mathbb{P}_{k-1}^+ \boldsymbol{\Phi}_k^\top + \mathbb{Q}(t) \tag{27}$$

where $\hat{\mathbf{x}}_k^-$ is the predicted state vector, $\mathbb{Q}$ - is the noise covariance matrix, $\mathbb{P}_k^-$ is the predicted states' covariance matrix, $\boldsymbol{\Phi}_k = \mathbb{I} + \mathbb{F}(x)\Delta t$, where $\Delta t = t_{\text{ctrl}} + t_{\text{meas}}$ is the control loop period, and $\mathbb{F}(x)$ is the Jacobian matrix of the vector $\mathbf{f}(\mathbf{x})$ with respect to the state vector $\mathbf{x}$,

$$\mathbb{F}\left(\hat{\mathbf{x}}_k^-\right) = \left.\frac{\partial \mathbf{f}(\mathbf{x})}{\partial \mathbf{x}}\right|_{\mathbf{x}=\hat{\mathbf{x}}_k^-} \tag{28}$$

For the problem in hand

$$\mathbb{F} = \begin{pmatrix} \mathbb{F}_{q\omega} & \mathbb{F}_{mb} \\ \mathbb{O}_{6\times6} & \mathbb{O}_{6\times6} \end{pmatrix}, \tag{29}$$

where $\mathbb{O}_{n\times n}$ is n by n matrix consisting of zeros, $\mathbb{F}_{q\omega}$ is 6 by 6 matrix obtained as the Jacobian matrix of the Equations (11) and (12) (see [6] for details and derivation), and, finally, $\mathbb{F}_{mb}$ is given by

$$\mathbb{F}_{mb} = \begin{pmatrix} \mathbb{O}_{3\times3} & \mathbb{O}_{3\times3} \\ \mathbb{J}^{-1}\mathbb{W}_{\mathbf{b}^B_{model}} & \mathbb{O}_{3\times3} \end{pmatrix}, \tag{30}$$

where $\mathbb{W}_{\mathbf{b}^B_{model}}$ is the skew-symmetric cross-product operator corresponding to vector $\mathbf{b}^B_{model}$.

Thus, the evolution matrix Φ is given by

$$\boldsymbol{\Phi} = \mathbb{I}_{12\times12} + \mathbb{F} \cdot (t_{ctrl} + t_{sens}). \tag{31}$$

Update

$$\mathbb{K}_k = \mathbb{P}_k^- \mathbb{H}_k^\top \left(\mathbb{H}_k \mathbb{P}_k^- \mathbb{H}_k^\top + \mathbb{R}_k\right)^{-1} \tag{32}$$

$$\hat{\mathbf{x}}_k^+ = \hat{\mathbf{x}}_k^- + \mathbb{K}_k \left[\mathbf{z}_k - \mathbf{h}\left(\hat{\mathbf{x}}_k^-, t_k\right)\right] \tag{33}$$

$$\mathbb{P}_k^+ = (\mathbb{I} - \mathbb{K}_k \mathbb{H}_k)\, \mathbb{P}_k^- \tag{34}$$

where $\hat{\mathbf{x}}_k^+$ is the updated state vector, $\mathbb{P}_k^+$ is the updated states' covariance matrix and $\mathbb{H}_k$ is the Jacobian matrix of the vector $\mathbf{h}(\mathbf{x})$ with respect to the state vector $\mathbf{x}$,

$$\mathbb{H}_k = \left.\frac{\partial \mathbf{h}(\mathbf{x})}{\partial \mathbf{x}}\right|_{\hat{\mathbf{x}}_k^-} \tag{35}$$

The observation model for a magnetometer-based filter is given by:

$$\mathbf{z} \approx \mathbf{h}(\mathbf{x}) = q^{BO} \circ \mathbf{b}^O_{model} \circ \tilde{q}^{BO} + \mathbf{b}^B_{res} \tag{36}$$

According to Equation (35), the observation matrix $\mathbb{H}_k$ is given by

$$\mathbb{H}_k = \begin{pmatrix} 2\mathbb{W}_{\mathbf{b}^B_{model}} & \mathbb{O}_{3\times6} & \mathbb{I}_{3\times3} \end{pmatrix}. \tag{37}$$

The $\mathbb{R}_k$ matrix is set constant according to

$$\mathbb{R}_k = \text{diag}\left(\begin{bmatrix} \sigma^2_{b_x}, & \sigma^2_{b_y}, & \sigma^2_{b_z} \end{bmatrix}\right) \tag{38}$$

where $\sigma^2_{b_x}$, $\sigma^2_{b_y}$ and $\sigma^2_{b_z}$ are the variances of measurement errors of the magnetic field in the local x, y and z of the sensor, which can be found in the magnetometer specifications.

Note: for better convergence it might be advisable to use unit vectors of the magnetometer measurements and magnetic field model in (36) – (38).

4. Simulation Results

The satellite orbit is assumed circular with an altitude of 400 km and inclination of 52°. The initial conditions are given by a random (normalized) quaternion and a random angular velocity (bounded by 5 deg/s 3σ). The inertia matrix for the CubeSat model is $J = \mathrm{diag}\,[14 \quad 15 \quad 7] \cdot 10^{-3}$ kg·m^2. The controller goal is to align the satellite's body-frame and the orbital frame. The controller gains are tuned to $k_\omega = 60 \cdot \omega_0^{-1}$ and $k_q = 12$ N · m · T^{-2}.

The available COTS magnetorquers restrict the magnetic dipole components to 0.2 $A \cdot m^2$ each in the nominal conditions. Each control loop consists of two parts - actuation and measurements, the duration of each part is $t_{ctrl} = 5s$ and $t_{sens} = 1s$.

The position of the magnetometer for which the parasitic magnetic field was evaluated in Section 2 is $(0, 0, -5.2)$ cm in reference to the body frame.

The magnetometer sensor noise is characterized by zero mean Gaussian white noise with a standard deviation $\sigma_{\text{magn}} = 200$ nT. Initial covariance matrix $\mathbb{P}_0$ is a diagonal matrix [12x12] with diagonal elements: $\sigma^2_{q_0}, \sigma^2_{q_0}, \sigma^2_{q_0}, \sigma^2_{\omega_0}, \sigma^2_{\omega_0}, \sigma^2_{\omega_0}, \sigma^2_{m_{res}}, \sigma^2_{m_{res}}, \sigma^2_{m_{res}}, \sigma^2_{B_{bias}}, \sigma^2_{B_{bias}}, \sigma^2_{B_{bias}}$, where σ_{q_0}, σ_{ω_0}, $\sigma_{m_{res}}$ and $\sigma_{B_{bias}}$ are assumptions of uncertainty in initial values for quaternions, angular velocities, residual magnetic moment and magnetometer bias respectively. In this study $\sigma_{q_0} = \pi/2$, $\sigma_{\omega_0} = 0.01$ rad/s, $\sigma_{m_{res}} = 0.1$ A·m^2, $\sigma_{B_{bias}} = 10^{-5}$ T. The EKF is initialized with the identity quaternion and zero angular velocity.

The environmental torques (except for the gravity-gradient torque, which is fully incorporated into the model of dynamics) are modeled here as a random torque represented by zero mean Gaussian white noise with a standard deviation $\sigma_{\text{trq}} = 3 \cdot 10^{-8}$ N·m.

4.1 *Controller Simulation Results*

The first simulation in this section is carried out in the absence of magnetic disturbances of any sort. Figure (9) shows the magnetic moment required by the controller (20)

It can be seen that after the initial transient period is over, the required magnetic moment never exceeds $2{\cdot}10^{-3}$ A·m^2. This is to signify how fine the magnetic control actually is. Let us also recall that the controller gains are tuned in accordance with a very particular procedure that involves linearization of the dynamics in the vicinity of the required regime and usage of Floquet theory [6]. Thus, the controller gains values cannot be raised just because it might seem that the controller's reaction to the attitude errors is small. To the best of our belief, the required magnetic moment as shown in the Figure 9 is actually nearly optimal. Having figured out, how much magnetic moment is needed for successful magnetic control, let us recall that the residual magnetic moment 3U CubeSats may range from 10^{-4} A·m^2 to 10^{-2} A·m^2 as per Reference[15]. Obviously, the problem of in-flight identification and compensation of residual magnetic moment along with providing the required control magnetic moment, seeing that the former may be greater than the latter by an order of magnitude, appears to be rather challenging.

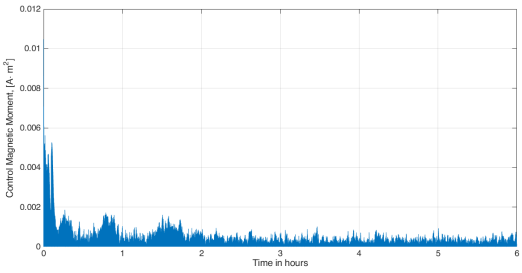

Fig. 9: Magnetic moment during the actuation

The level of control magnetic moment shown in Figure (9) also sets the limit to the admissible level of residual magnetization, which clearly cannot exceed 10^{-3} A·m^2 if we are to hope to preserve the controllability of the system. The reasoning behind this estimate is that in case the torque due to residual magnetization and the control torque are of the same order of magnitude then for a 10% error of $\mathbf{m}_{res}$ estimation by EKF the uncompensated disturbance is by an order of magnitude less than the control torque. If this ratio is not exceeded our numerical experiments show that the control authority is still preserved.

This estimate is important for the second step in the pipeline of our magnetic cleanliness program. That is, when the magnetic model is built and verified by measurements, the decision whether or not some of the satellite's components need to be redesigned is made on the base of the threshold value obtained here.

4.2 *Constant Magnetic Disturbance*

Let us now estimate, how great a residual magnetic moment can be for the previously described controller to be able to compensate it. We shall assume that the controller's performance is acceptable, when the pointing error after the system is settled does not exceed 15°. The threshold actually takes its origin

from the Swarm mission requirements mentioned in the Introduction.

The setup for this numerical experiment is as follows. We shall add to the system a certain constant value of residual magnetic moment $\mathbf{m}_{\text{res}}$. The direction of this vector shall be constant throughout all simulations carried out in this experiment and defined as $\mathbf{e}_m = [1 \quad 1 \quad 1]^\top / \sqrt{3}$, and the magnitude shall be varied to test the controller's limits.

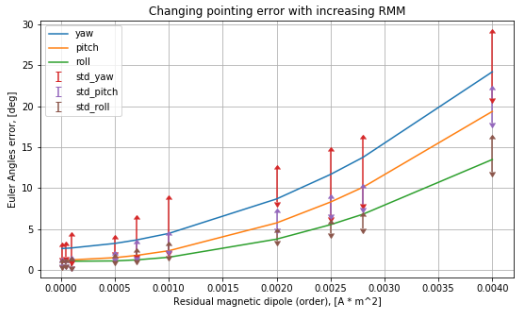

Fig. 10: The control quality degradation with increasing of the residual magnetic moment

Simulation results for identification and rejection of a constant magnetic moment and the corresponding magnetometer bias are shown in (Fig. 10). Each point in the plot of (Fig. 10) represents 30 simulations (with random initial conditions). The ordinate values correspond to the mean RMSE of the Euler angles after the system has settled. Error bars correspond to standard deviations calculated for each point. It can be seen that the performance threshold expressed through Euler angles is still not exceeded when the magnitude of residual magnetic moment is at $2.5 \cdot 10^{-3}$ A·m^2, which agrees with the earlier estimates (see Fig. 9).

The graphs in Fig. 11 - 13 show the detailes for an example simulation with residual magnetic moment of $2.5 \cdot 10^{-3} A \cdot m^2$. The initial conditions for the example run are:

$$q^{OB}(0) = (0.157, 0.693, 0.593, 0.378)\,,$$
$$\omega(0) = (0.01, 0.01, 0.01)\,\text{rad/s}.$$

Fig. 11 shows the controller convergence for the maximum admissible constant magnetic disturbance with the errors in all three Euler angles bounded by 15° threshold. The graphs in Fig. 12 and Fig. 13 show relative errors of the residual magnetic moment and the magnetometer bias estimates by EKF, which are about bounded by 6% and 20%, respectively. Let us note in this experiment we model magnetic disturbance using the residual magnetic dipole model and thus can compare its modeled and estimated values.

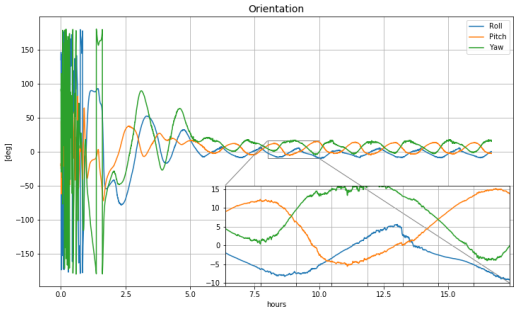

Fig. 11: Pointing accuracy in case of constant residual magnetic disturbances

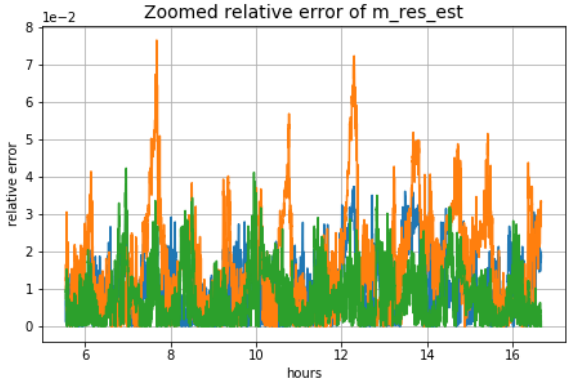

Fig. 12: Relative error in magnetic moment estimation

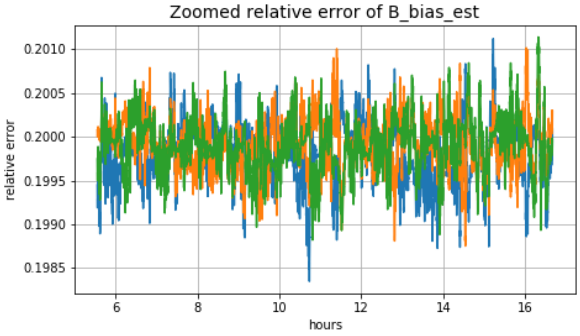

Fig. 13: Relative error in magnetometer bias estimation

4.3 *Varying Magnetic Disturbance*

Now let us evaluate the system's performance using the model of residual magnetization described earlier. For this experiment we shall take assume the torque matrices and parasitic magnetic field values obtained in Section 2, although rescaled to satisfy the limits set in Section 4.1.

Tracking a slowly varying magnetic disturbance. This numerical experiment is to test the EKF performance in the presence of slowly varying magnetic disturbance caused by the spacecraft rotation and, consequently, changes of the incident angles of sunlight for every solar panel. The results in terms of the torque due to magnetic disturbance and controller convergence in terms of Euler angles are presented in Fig. 14 and 15, respectively.

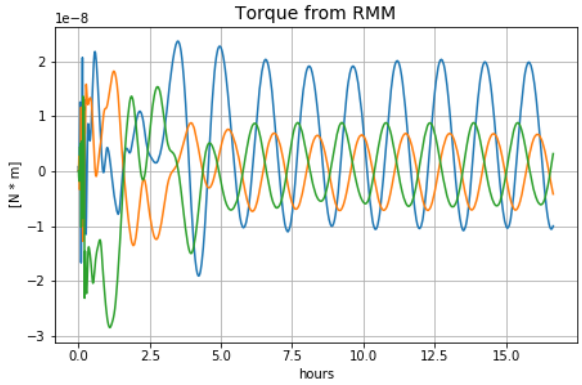

Fig. 14: Varying torque with time due to the sun incidence angle on solar panels

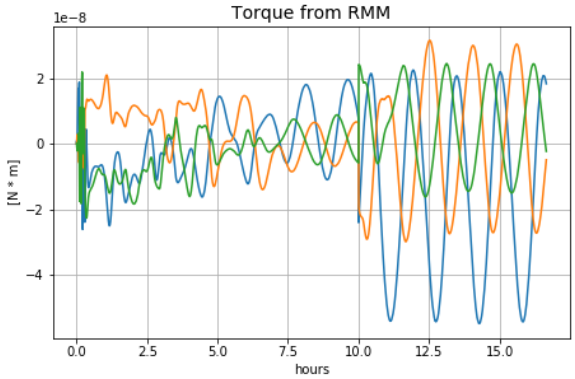

Fig. 16: Varying torque with time due to abrupt changes in the regime at about 10h

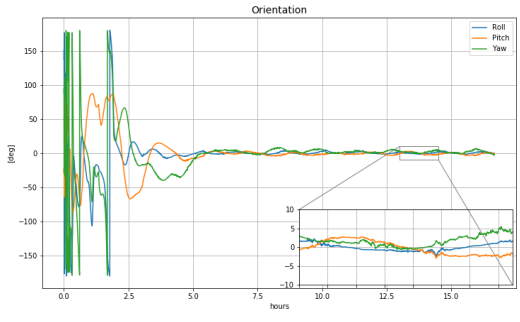

Fig. 15: Pointing accuracy in case of varying magnetic disturbances due to the sun incidence angle on solar panels

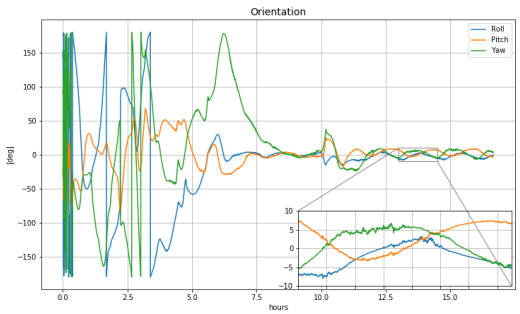

Fig. 17: Pointing accuracy in case of abrupt changes in the regime at about 10h

The magnetic moment to which the filter converged is estimated as $\mathbf{m}_{res} \approx 5 \cdot 10^{-4}$ A·m^2 and magnetometer bias is about $7.7 \cdot 10^{-6}$ T. The pointing accuracy for this particular example is about 5 degree, which agrees with the earlier simulations for constant residual magnetic moment. The conclusion we draw is that the filter successfully tracks varying magnetic disturbance.

Recuperating after abrupt changes in magnetic disturbance. In this numerical experiment we shall demonstrate the reaction of the control system to an abrupt change in the magnetization regime (which is simulated by inclusion of another source of magnetization into equation (15)). Furthermore, we shall also show how a map value for torque due to magnetic disturbances and magnetometer bias are obtained, and how using a map with this values makes the system more robust.

Fig. 16) shows the torque due to magnetic disturbances. It is seen that at $t = 10$ hr there is an abrupt

change in the level of disturbance caused by a regime change.

The reaction of the control system to the regime change is show in Fig. **??**. The filter has converged before the change took place, but at $t = 10$ hr it could not track the change in the estimated parameters. As a result the control accuracy degraded to 20-30 degrees, and it took almost 2 hours for the system to regain control authority.

It is important to note that after these two hours EKF recovered and converged to new estimates of residual magnetic moment and magnetometer bias as shown in Fig. 18,19). These values can be saved as a map for the new regime, which can be further used to provide an initial approximation for the magnetic disturbance parameters should this regime be switched on again. Obtaining these maps for all principal regimes is equivalent to having an atlas of magnetic disturbances.

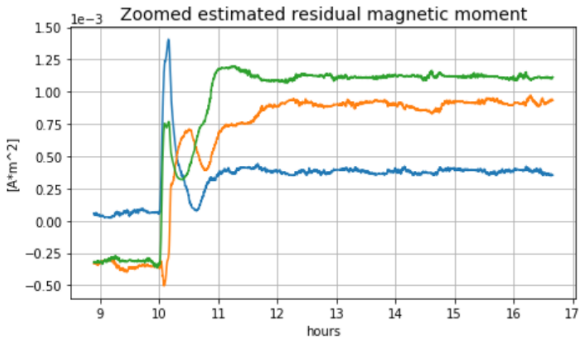

Fig. 18: Estimated zoomed values of residual magnetic moment in case of abrupt changes in the regime at about 10h

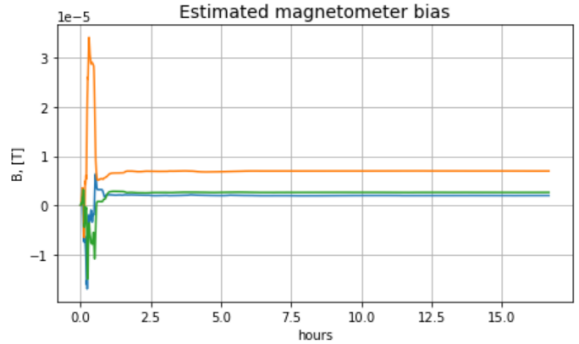

Fig. 19: Estimated values of magnetometer bias in case of abrupt changes in the regime at about 10h

We shall now repeat the same experiment with the only difference of making the control system prepared for the rapid change in the residual magnetization level. This time as soon as we switch between the regimes that as we have found out are characterized by significantly different magnetic disturbances, we shall feed a magnetic map to the EKF and see its reaction to it. By feeding the map to the filter we imply using the values it converged to during the previous experiments to update the corresponding variables in the prediction step of the EKF.

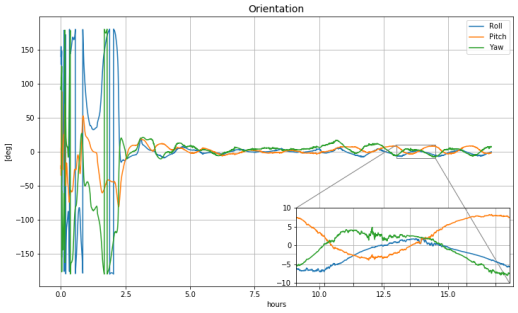

Fig. 20: Pointing accuracy in case of abrupt changes in the regime at about 10h and feeding the atlas of pre-estimated changes

Fig. 20 shows how the control system passes through an abrupt regime change. It is seen in the Euler angle plots that there is a reaction and the control quality becomes worse, but only to the extent corresponding to the increased level of disturbance. It is but one example, however, our numerical experiments show that in-flight usage of the magnetic disturbance atlases are indeed advantageous and allow spacecraft a certain degree of autonomy for overcoming magnetic disturbances. Furthermore, such atlases need and can be updated during the spacecraft's lifetime, which can also be performed autonomously.

5. Conclusion

This study considers the design of a CubeSat and in-flight performance of its attitude control system with magnetic actuation in the presence of disturbances caused by residual magnetization. It is shown that the magnetic field produced through PCBs and solar panels poses a significant value and should be monitored over each operation regime of the satellite to create an atlas of magnetic disturbances. Our numerical experiments show that such atlas does enhance EKF performance in terms of preserving con-

trol authority over the spacecraft even during abrupt changes of the disturbance levels. This paper presented a magnetometer-based EKF, however, as a future study we are going to fuse other sensors (gyros and sun sensors) with the magnetometer to see if this will make the control system more robust.

References

[1] A. Annenkova, S. Biktimirov, K. Latyshev, A. Mahfouz, P. Mukhachev, and D. Pritykin. Cubesat adcs model for preliminary design procedures within a concurrent design approach. *AIP Conference Proceedings*, 2171, 2019.

[2] Anastasiia Annenkova, Anton Afanasev, and Dmitry Pritykin. Revisiting the residual magnetization problem in cubesat magnetic attitude control. *Advances in the Astronautical Sciences*, 2020. (in print).

[3] M. Dougherty, S. Kellock, D. Southwood, Andre Balogh, E. Smith, B. Tsurutani, B. Gerlach, K.-H Glassmeier, F. Gleim, C. Russell, G. Erdos, F. Neubauer, and S. Cowley. The cassini magnetic field investigation. *Space Science Reviews*, 114:331–383, 09 2004.

[4] T. Guillod. Gerber to ODB PCB tracks converter for COMSOL (unmaintained). https://in.mathworks.com/matlabcentral/fileexchange/36014-gerber-to-odb-pcb-tracks-converter -for-comsol-unmaintained, 2020.

[5] T. Inamori, N. Sako, and S. Nakasuka. Magnetic dipole moment estimation and compensation for an accurate attitude control in nanosatellite missions. *Acta Astronautica*, 68(11-12):2038–2046, 2011.

[6] DS Ivanov, M Yu Ovchinnikov, VI Penkov, DS Roldugin, DM Doronin, and AV Ovchinnikov. Advanced numerical study of the three-axis magnetic attitude control and determination with uncertainties. *Acta Astronautica*, 132:103–110, 2017.

[7] A. Lassakeur and C. Underwood. Magnetic cleanliness program on cubesats for improved attitude stability. pages 123–129, 2019.

[8] Wilfried Ley, Klaus Wittmann, and Willi Hallmann. *Handbook of space technology*, volume 22. John Wiley & Sons, 2009.

[9] M. Ludlam, V. Angelopoulos, E. Taylor, R. C. Snare, J. D. Means, Y. S. Ge, P. Narvaez, H. U. Auster, O. Le Contel, D. Larson, and T. Moreau. *The THEMIS Magnetic Cleanliness Program*, pages 171–184. Springer New York, New York, NY, 2009.

[10] A. Mahfouz, D. Pritykin, A. Afanasev, A. Annenkova, and K. Latyshev. Coordinated attitude determination and control in a swarm of cubesats. *Proceedings of the International Astronautical Congress, IAC*, 2019-October, 2019.

[11] Masaki Matsushima, Hideo Tsunakawa, Yuichi Iijima, Satoru Nakazawa, Ayako Matsuoka, Shingo Ikegami, Tomoaki Ishikawa, Hidetoshi Shibuya, Hisayoshi Shimizu, and Futoshi Takahashi. Magnetic cleanliness program under control of electromagnetic compatibility for the selene (kaguya) spacecraft. *Space science reviews*, 154(1-4):253–264, 2010.

[12] Dmitry Pritykin, Sergey Efimov, and Vladislav Sidorenko. Defunct satellites in nearly polar orbits: Long-term evolution of attitude motion. *Open Astronomy*, 27(1):264 – 277, 01 Nov. 2018.

[13] ECSS Secretariat. Ecss-e-hb-20-07a. *Space Engineering–Electromagnetic Compatibility Handbook, ESA-ESTEC. Noordwijk, The Netherlands: Requirements & Standards Division*, 2012.

[14] Goo-Hwan Shin, Dong-Guk Kim, Se-Jin Kwon, and Hu-Seung Lee. Analysis of magnetic dipole moment for a 300-w solar-cell array. *Journal of Astronomy and Space Sciences*, 36(3):181–186, 2019.

[15] John Springmann, James Cutler, and Hasan Bahcivan. Magnetic sensor calibration and residual dipole characterization for application to nanosatellites. In *AIAA/AAS Astrodynamics Specialist Conference*. American Institute of Aeronautics and Astronautics, 2010.